Dynamic label-free imaging of lipid droplets and their link to fatty acid and pyruvate oxidation in mouse eggs.

Authors: Josephine Bradley[1], Iestyn Pope[1], Yisu Wang[1], Wolfgang Langbein[2], Paola Borri[1] and Karl Swann[1]*

[1] School of Biosciences, Cardiff University, The Sir Martin Evans Building, Museum Avenue, Cardiff, CF10 3AX,
[2]School of Physics and Astronomy, Cardiff University, The Parade, Cardiff, CF24 3AA

*To whom correspondence should be addressed at: School of Biosciences, Cardiff University, The Sir Martin Evans Building, Museum Avenue, Cardiff, CF10 3AX;
SwannK1@cardiff.ac.uk . Tel 02920 879009.
http://www.cardiff.ac.uk/people/view/126754-swann-karl

Other author emails:
Josephine.bradley@southwales.ac.uk
PopeI@cardiff.ac.uk
WangY150@cardiff.ac.uk
LangbeinWW@cardiff.ac.uk
BorriP@cardiff.ac.uk

Key words: Egg, CARS, β-oxidation, lipid droplets, deuterated lipids

Summary Statement

Lipid droplets reorganise in mouse eggs and maintain a dynamic balance oxidation of fatty acids and pyruvate.

JCS Advance Online Article. Posted on 10 June 2019

Summary

Mammalian eggs generate most of their ATP by mitochondrial oxidation of pyruvate from the surrounding medium, or from fatty acids which are stored as triacylglycerols within lipid droplets. The balance between pyruvate and fatty acid oxidation in generating ATP is not established. We have combined coherent anti-Stokes Raman scattering (CARS) imaging with deuterium labelling of palmitic acid to monitor turnover of fatty acids within lipid droplets of living eggs. We found that loss of labelled palmitic acid is promoted by pyruvate removal, but minimised with inhibited β-oxidation. Pyruvate removal also causes a significant dispersion of lipid droplets, while inhibiting β-oxidation causes droplet clustering. Live imaging of luciferase, or FAD autofluorecence from mitochondria, suggest that inhibiting β-oxidation in mouse eggs only leads to a transient decrease in ATP because there are compensatory uptake of pyruvate into mitochondria. Inhibiting pyruvate uptake and then β-oxidation caused similar and successive declines in ATP. Our data suggest that β-oxidation and pyruvate oxidation contribute nearly equally to resting ATP production in mouse eggs and that reorganisation of lipid droplets occurs in response to metabolic demand.

Introduction

Ovulated mouse eggs (metaphase II arrested oocytes) depend almost entirely upon their ~100,000 mitochondria for ATP production via oxidative phosphorylation (Dumollard *et al.* 2004). Mitochondria continue to supply most ATP during the early cleavage divisions because glycolytic activity is low in mammalian embryos until the morula or blastocyst stages (Downs, 1995). Substrates such as pyruvate and fatty acids are taken up into and oxidised within the mitochondria. Pyruvate is provided by the follicular fluid and glycolytic cumulus cells surrounding the developing egg within the ovarian follicle (Downs, 1995), while *in vitro*, pyruvate is supplemented within the culture media.

Fatty acids are also taken up into the egg from the follicular fluid and may reside as free fatty acids within the cytosol, or they are densely stored as triacylglycerols (TAGs) within vesicles known as lipid droplets (LDs) (Homa *et al.* 1986). The composition of LDs seems to be similar between different species (Bradley 2016 ; McEvoy *et al.* 2000). Although it is well established that mammalian eggs oxidise both pyruvate and fatty acids, the balance between these substrates is unclear. Some species such as pigs, dogs and cows have a substantial amount of lipid in the form of large LDs in their cytoplasm that gives them a dark appearance under optical transmission microscopy (Sturmey and Leese, 2003; Apparicio *et al.* 2012). In contrast, mouse and human eggs have a more transparent cytoplasm, and for mouse eggs this is clearly associated with a much reduced lipid content (Bradley *et al.* 2016).

Pyruvate is the primary essential energy source for developing mouse and human eggs/embryos (Gardner and Leese, 1986). Starving mouse eggs of pyruvate, using mitochondrial uptake inhibitors, such as cinnamate derivatives, greatly affects the egg's developmental potential (Dumollard *et al.* 2007). Luminescence imaging of ATP levels using injected firefly luciferase has been used to show that eggs deprived of substrates exhibit reduced ATP and that only pyruvate, and not glucose, glutamine or lactate, can restore ATP levels (Dumollard *et al.* 2008). Pyruvate uptake and the stimulation of egg mitochondrial metabolism can also be specifically monitored by measuring the FAD (green) autofluorescence (Dumollard *et al.* 2004). FAD is bound to flavoproteins in the mitochondria and the FAD/$FADH_2$ ratio reflects the redox state of mitochondria (Dumollard *et al.* 2004). Both luciferase imaging of ATP and autofluorescence imaging of FAD have been used to demonstrate Ca^{2+} induced increase in $FADH_2$ and ATP production in mouse egg mitochondria during the Ca^{2+} oscillations at fertilisation (Dumollard *et al.* 2004). These methods have thus far not been used to investigate lipid metabolism in mouse eggs.

Despite the recognised role of pyruvate metabolism in supporting mouse embryo development it has become clear that fatty acid oxidation is also significant. Dunning *et al.* showed that mouse embryos metabolise palmitic acid and that the promotion of β-oxidation using L-carnitine to facilitate fatty acid transport into mitochondria resulted in increased egg quality, fertilisation and blastocyst rates (Dunning *et al.* 2011). The same group also demonstrated that inhibiting β-oxidation via mitochondrial uptake inhibitor etomoxir, impaired blastocyst development (Dunning *et al.* 2010). Hence, mitochondrial fatty acid oxidation may also contribute to energy production in mouse eggs and early embryos, despite their low lipid content. However, it is not clear what fraction of ATP production might originate from fatty acid β-oxidation. It is also not known whether fatty acid oxidation utilises fatty acid derived from endogenous LDs or exogenous sources. One limitation is that real-time imaging methods for investigating LD and fatty acid metabolism in eggs and embryos are not as well-developed as those for monitoring cytosolic or mitochondrial redox state, or ATP production. Destructive chemical analysis of lipids does not allow for the assessment of spatial and dynamic events.

We have previously demonstrated the use of coherent anti-Stokes Raman scattering (CARS) microscopy for the quantification of the number, spatial distribution and chemical content of LDs in mouse eggs and embryos without compromising the viability of the egg (Bradley *et al.* 2016). CARS microscopy is label-free and chemically specific (Potma and Xie, 2004). It is based on the phenomenon of Raman scattering, namely the interaction of light with vibrating chemical bonds which produces light scattered at a different wavelength (hence color) compared to the incident light. The wavelength shift is a direct signature of the frequency of the vibration, which in turn depends on

the type of chemical bond. Although this scattering phenomenon usually produces a very weak signal, it can be enhanced when two short laser pulses are used to coherently drive the vibrations. In this way, the scattered light from all bonds of the same type in the focal volume constructively interferes, generating CARS that can be acquired at high speed for chemically-specific live cell imaging applications. CARS is very effective when imaging lipids since they contain a large number of identical CH_2 bonds in the aliphatic chain, and lipid molecules are densely packed inside LDs. CARS also provides intrinsic three-dimensional spatial resolution without the need of a confocal detection pin-hole, as the nonlinear process only takes place within the focal volume, where high photon densities are reached. In our previous work (Bradley *et al.* 2016) we quantified the number, size, and aggregation patterns of LDs within the cytoplasm of live mouse eggs. The amplitude of the CARS signal from each droplet also allowed us to assess the total lipid content, as the number of CH_2 bonds within the focal volume is proportional to the square root of the CARS intensity. CARS imaging of eggs and early embryos at the CH_2 vibrational resonance ($2850cm^{-1}$) showed that LD distribution and size changed as development continued. It was shown that immature GV eggs displayed LDs spatially dispersed throughout the cytoplasm, while LDs in the mature MII egg exhibited a more 'clustered' configuration, with LD aggregates. These studies showed that CARS imaging can be used to characterise LD spatial patterns and lipid content in live eggs and embryos.

As well as probing the CH_2 vibrational resonance, CARS microscopy can be used to excite and monitor carbon-deuterium bonds (Potma and Xie, 2004; Bergner *et al.* 2011). Due to the heavier isotopic mass, deuterated bonds have a lower vibrational resonance compared to their hydrogen counterpart, providing a recognisable CARS signal first demonstrated by Duncan *et al.* with the detection of the deuterium-oxygen bond (D-O) in deuterated (heavy) water (D_2O) at the $2450cm^{-1}$ frequency (Duncan *et al.* 1982). For lipids, the CD_2 bond symmetric stretch vibration has a CARS peak at $2140cm^{-1}$, distinctly separated from the CH_2 vibrational mode at $2850cm^{-1}$. Notably, it also has a different vibrational frequency to other cellular components, and lies within the otherwise 'silent' region of the CH_2 lipid Raman spectral profile (see Fig.1). Thus, deuterium-labelled lipids can be selectively imaged with CARS, well-separated from naturally-occurring lipids within cells (Rodriguez *et al.* 2006). Deuterated palmitic acid has previously been shown to be taken up into LDs within CHO cells and whole nematodes, using Stimulated Raman spectroscopy (SRS) (Zhang *et al.* 2011; Fu *et al.* 2014), but experimental investigation of turnover of labelled fatty acids has not been carried out.

In this paper, we use CARS microscopy to investigate how the LD spatial distribution in mouse eggs relates to the extent of mitochondrial metabolism occurring within the cell. We find that starving eggs of pyruvate leads to a wide dispersion of LDs, while inhibiting β-oxidation leads to an increased clustering of LDs. We employ deuterated-oleic acid (D-OA) to specifically and unambiguously assess the storage and use of fatty acids within the mammalian egg. We show how the rate loss of deuterium

labelling of LDs is increased by removal of pyruvate as a substrate, while inhibition of β-oxidation maintains the amount of D-OA within the egg. Using live cell imaging of luciferase luminescence we find that inhibiting β-oxidation only leads to a transient decrease in ATP levels. Using the autofluorescence of FAD, we then show that inhibiting fatty acid oxidation leads to an unexpected decrease in FAD (increase in $FADH_2$), likely due to compensatory uptake of pyruvate, which could explain why ATP levels are restored in the absence of β-oxidation. Our data suggest that β-oxidation contributes ~50% of the mitochondrial ATP production in eggs and that this is in dynamic balance with pyruvate oxidation.

Results

Lipid droplet distribution reflects metabolic state

As we have shown previously (Bradley *et al.* 2016), CARS microscopy at the CH_2 symmetric stretch vibration (2850cm^{-1}), abundant in the acyl chain of fatty acids, allows label-free chemically specific imaging of lipid droplets in live cells. LDs in MII eggs cultured in simple M2 medium present a spatial distribution where they are seen in multiple small clusters throughout the cell cytoplasm (Fig.2D). It is notable that these clusters are also apparent in high-resolution differential interference contrast (DIC) images (Fig.2A) and can be chemically identified using CARS microscopy. Starving MII eggs of carbohydrate and glutamine, via incubation in HKSOM lacking pyruvate, lactate, glutamine and glucose for ~6 hours prior to CARS imaging, leads to wide spatial dispersion of the LDs throughout the whole egg (Fig.2E). This is also identifiable via the lack of clusters seen using high resolution DIC (Fig.2B). In contrast, inhibition of β-oxidation with 100μM etomoxir for ~6hrs prior to CARS imaging, causes a LD distribution somewhat exaggerated from the norm, appearing to have an increased number and size of LD clusters (Fig.2F). Again, these changes are also apparent in images taken with DIC (Fig.2C).

Quantitative analysis of the aggregate patterns within these eggs was performed as described by Bradley *et al.* (2016). Briefly, a LD was considered being part of a 'cluster' when the LD centre spatial position was within a distance of 1.5 x the resolution (0.3μm laterally, 0.6μm axially) to that of the nearest neighbouring droplet (Fig.2J). Each droplet determined to be within the same cluster was given the same index value. The occurrence of such index was then used to count the number of LDs in one cluster, which we call cluster (or aggregate) 'size'. The occurrence of aggregate sizes was then obtained, as shown in the histograms in Fig.2G-I. MII eggs demonstrate numerous clusters of >10 LDs, with only 59.5% (±14.4 SD) of LDs in an un-clustered, isolated position (Fig.2G). Carbohydrate-starvation leads to the total lack of clusters of >10 LDs, with 84.1% (±10.8 SD) of LDs isolated (Fig.2H). Inhibition of β-oxidation causes LDs to aggregate into more clusters, of higher numbers of LDs than typically seen in a normal MII egg, with only 38.4% (±14.9 SD) isolated LDs (Fig.2I). The extent of LD aggregation was calculated as the square root of the mean square aggregate

size ($\sqrt{\langle s^2 \rangle}$) per egg (see Experimental Methods), and then the average $\sqrt{\langle s^2 \rangle}$ per population of eggs under each condition was plotted, as seen in Fig.2K. This analysis confirms that significantly fewer clusters are seen in a carbohydrate-starved egg (green triangle, Fig.2K), compared to an egg subjected to β-oxidation inhibition (blue inverted triangle, Fig.2K). Normal MII (red circle, Fig.2K) and β-oxidation-inhibited MII LD distributions are seen to be different from a random distribution of LDs. This is exemplified in Fig.2K (violet hexagon, yellow star, dark blue pentagon) where we calculated the occurrence of LD clusters and in turn $\sqrt{\langle s^2 \rangle}$ by simulating a completely random distribution of either 2000, 4000, or 6000 droplets in the same egg volume, respectively. These data suggest that the degree of LD clustering reflects whether carbohydrates or fatty acids are being oxidised by mitochondria.

Dynamic imaging of endogenous fatty acid turnover

Mouse eggs can survive and maintain some ATP production for many hours in media without carbohydrates (Dumollard *et al.* 2004; Dumollard *et al.* 2008). This implies that mitochondria metabolise endogenous substrates such as fatty acids stored in LDs. We sought to monitor this using deuterated lipids. Deuterated carbon (CD_2) is abundant in deuterated fatty acids and gives rise to a resonant CARS intensity frequency shifted from the CH_2 stretch vibration (Fig.1). Therefore, deuterated fatty acids can be used as a non-invasive 'label' for CARS imaging in order to examine how specific fatty acids are stored into LDs or metabolised from them. Notably, from the CARS intensity strength we can quantitatively examine whether deuterated fatty acid accumulation is gained with incubation, or lost with metabolism.

GV oocytes were *in vitro* matured in maturation medium containing 400μM deuterated oleic acid (D-OA). CARS imaging of the resulting MII eggs at the CD_2 vibration peak (2140cm^{-1}), and the CH_2 vibration (2850cm^{-1}) clearly demonstrates that D-OA is taken up into the cell from the surrounding medium during maturation and is stored as TAGs in LDs, providing a high CARS intensity (Fig.3B, and Table 1), albeit lower than the signal from non-deuterated fatty acids at the CH_2 peak (Fig.3C, and Table 1). Uptake is further demonstrated with comparison of a D-OA-matured egg with a control egg *in vitro* matured without D-OA (Fig.3E, and Table 1). Imaging at the CD_2 vibrational mode in an MII egg matured without D-OA shows that the control egg provides a lower CARS intensity (albeit not zero, due to the non-resonant CARS contribution) than a D-OA-incubated egg, whereas the CARS intensity at the CH_2 peak in the same egg (Fig.3F, and Table 1) is considerably higher. Examples of CARS spectra of individual LDs acquired using the hyperspectral imaging modality available in the microscope (Pope et al., 2013) show the CD_2 vibrational peak alongside the CH_2 stretching band characteristic of lipids (Supplementary Figure S1). These data show that CARS imaging can detect deuterated oleic acid taken up by LDs in live mouse eggs.

Extended culture of D-OA-matured eggs in M2 medium for ~6hrs allows us to see the loss of D-OA label over time, and thus the physiological turnover of fatty acids within the egg. Fig.4B shows that the CARS signal intensity at the CD_2 peak ($1.05x10^7$ photoelectrons ($ph.e^-$)/sec) is roughly half that of an MII egg immediately after maturation in D-OA (time 0, $2.09x10^7$ $ph.e^-$/sec, Fig.3B). While the CARS signal at the CH_2 peak remains higher than at CD_2 ($2.78x10^7$ $ph.e^-$/sec, Fig.4C), the signal is still lower than seen for CH_2 at time 0 ($3.07x10^7$ $ph.e^-$/sec, Fig.3C). Incubation of D-OA-matured eggs alongside carbohydrate-starvation for ~6hrs before CARS imaging leads to the exaggerated loss of CARS signal, at both the CD_2 ($0.65x10^7$ $ph.e^-$/sec, Fig.4E) and CH_2 peaks ($1.21x10^7$ $ph.e^-$/sec, Fig.4F). The loss of D-OA appears to be in the same order as, if not lower than, the control MII egg matured without D-OA ($0.83x10^7$ $ph.e^-$/sec, Fig.3E). In contrast, culturing D-OA-matured eggs alongside inhibition of β-oxidation with 100μM etomoxir for ~6hrs prior to CARS imaging (Fig.4G-I) shows CD_2 and CH_2 CARS intensities similar to those seen immediately after maturation (time 0, Fig.3B). These data are summarised in Table 1.

To better quantify these results, the average D-OA volume per LD ($\langle v \rangle$) was calculated (see Experimental Methods) for all eggs under each condition described. This was then plotted in order to quantitatively compare the loss of D-OA signal after alteration of β-oxidation (Fig.5). Incubation with carbohydrate-starvation causes a significant loss of D-OA label (pink triangle), comparable to control eggs matured without D-OA (green diamond). Incubation with etomoxir causes little or no decrease in CARS signal (red circle) from the level seen in control eggs imaged immediately after D-OA maturation (black square). After ~6hrs incubation in simple M2 medium, eggs appear to lose D-OA label, demonstrating physiological fatty acid turnover (blue triangle), but this is not significantly different to control eggs. These data show that loss of deuterated oleic acid from LDs can be imaged in mouse eggs in a way that is consistent with endogenous β-oxidation. This in turn implies β-oxidation is enhanced during carbohydrate starvation. These data are again summarised in Table 1.

Contribution of β-oxidation to mitochondrial redox potential

The above data suggests that mouse eggs switch to using β-oxidation from endogenous fatty acid stores when pyruvate is not available. However, it is unclear how much β-oxidation is contributing to the overall mitochondrial metabolism in the egg in normal medium. FAD autofluorescence can be used as a measure of the redox state of mitochondria in eggs (Dumollard *et al.* 2004). Addition of 100μM etomoxir, to inhibit β-oxidation, in mouse eggs caused a marked decrease in FAD signal (Fig.6A), with a slight oscillation before settling to a new, lower (more reduced) FAD level. The redox state of FAD in mitochondria can be calibrated by addition of cyanide and FCCP (1). Addition of 2mM cyanide (CN^-) prevents the reduction of oxygen in the electron transport chain (ETC), inducing a maximally reduced ($FADH_2$) redox state (Fig.6B), while addition of 1μM uncoupler

FCCP, after perfusion of fresh media, causes maximum oxidation (Fig.6C). This calibration of the FAD autofluorescence signal allows the contribution of fatty acid oxidation to be assessed. By comparing the starting value of the FAD fluorescence with the maximal and minimum fluorescence values obtained in cyanide and FCCP we can estimate that the MII mouse egg mitochondria are at 60.5% (±3.1 SEM) of their total redox potential. In addition, from the change in FAD fluorescence induced by etomoxir we can estimate β-oxidation contributes 49.8% (±2.7 SEM) of the starting or 'resting' mitochondrial FAD/$FADH_2$ redox state. It should be noted that the effects of etomoxir were specific to mitochondrial flavoproteins because addition of etomoxir after FCCP or cyanide treatment of eggs cause no change in autofluorescence (Fig.S2).

Contribution of β-oxidation and pyruvate metabolism to ATP production

The FAD/$FADH_2$ couple in mitochondria gives an indication of mitochondrial metabolism but we also wanted to examine the immediate effect on ATP production of interfering in β-oxidation. To monitor the relative ATP levels in eggs we microinjected firefly luciferase and the luminescence was measured in eggs incubated in HKSOM medium containing 100μM luciferin (Dumollard *et al.* 2008). Inhibition of β-oxidation with the addition of 100μM etomoxir during imaging caused a transient decrease in luminescence, before a recovery to similar levels of luminescence at the start of recording (Fig.7A). This suggests that eggs require β-oxidation for maintaining ATP levels, but that they can rapidly compensate for reduced β-oxidation previous resting ATP. Mitochondrial pyruvate uptake can be inhibited in mouse eggs by addition of 500μM cinnamate during imaging. We found that this also leads to a decrease in the production of ATP (Fig.7B(i)). However, the subsequent inhibition of β-oxidation with etomoxir leads to a further ATP decrease which, interestingly, does not recover as seen when added without prior pyruvate starvation (Fig.7B(ii)). These data suggests that pyruvate uptake is required for eggs to maintain ATP levels in the absence of β-oxidation. From the size of the relative changes in luciferase luminescence it also appears that ~50% of the resting ATP in an MII egg is attributable to β-oxidation.

A conventional luminescent assay of whole cell ATP was also performed in mouse eggs by lysing eggs in buffer and measuring luminescence in a luminometer. The luminescence signal emitted by eggs was calibrated with recombinant firefly luciferase to provide an amount of ATP per egg. We found that a control MII mouse egg has ~3.5mM ATP (Fig.7C(i)). Inhibition of β-oxidation with 100μM etomoxir does not appear to change the whole cell ATP after 1 hour's incubation (Fig.7C(ii)), nor does starvation of pyruvate for 1 hour using either 500μM cinnamate or incubation in media lacking pyruvate, lactate, glucose and glutamine (Fig.7C(iii)). However, incubation of eggs with simultaneous β-oxidation inhibition and carbohydrate starvation dramatically decreases the amount of ATP seen in whole cells after 1 hour (Fig.7C (iv)). Incubation in 1μM FCCP demonstrates the lowest amount of ATP reached (Fig.7C(v)). These data are consistent with the results seen with the dynamic luciferase assay of ATP shown in Fig.7A and B in that only a combination of inhibiting both pyruvate

and fatty acid oxidation by mitochondria leads to a significant decrease in ATP in mouse eggs. The data support the idea that pyruvate uptake can compensate for loss of β-oxidation in generating ATP.

Discussion

It is widely accepted that pyruvate is the principal mitochondrial substrate for mouse or human eggs (Dumollard *et al.* 2009). However, in recent years it has become clear that mitochondrial fatty acid oxidation in mouse eggs and early embryos is also important in affecting their developmental viability (Dunning *et al.* 2010; 2011). Here, we show that LDs change their spatial distribution when carbohydrates are unavailable and that we can image the metabolism of fatty acids in LDs in live eggs using CARS microscopy and deuterium-labelled fatty acids. We also provide evidence that β-oxidation provides a substantial contribution to both the ATP output, and the resting redox state of the MII mouse egg.

The metabolic state of the mammalian egg or embryo is indicative of its developmental potential (Leese, 2002; Leese *et al.* 2016). We have now found that the level of β-oxidation occurring in the egg is reflected in its LD distribution. It appears that when the LDs are in a distinctly clustered arrangement, fatty acid oxidation is occurring at a lesser level, while pyruvate oxidation is likely dominant. Conversely, LDs widely-dispersed throughout the cytoplasm signify an increased capacity for β-oxidation, where pyruvate may be limited. It is likely that LDs disperse in order to increase the surface area available for fatty acid mobilisation, while clustering may be indicative of energy conservation and it may be that these eventually coalesce into larger LDs as seen at the morula and blastocyst stages of later pre-implantation embryo development (Bradley *et al.* 2016). It is notable that whilst a number of proteins involved in LD fusion have been described, the mechanism of clustering which may act as a prelude to fusion, has not been established (Walther and Farese, 2012).

Deuterium labelling of LDs using the cell's ability to incorporate deuterated oleic acid has allowed dynamic visualisation of fatty acid turnover. Oleic acid has been shown to promote the formation of TAGs and lipid storage as LDs in eggs (Zhang *et al.* 2011; Shaaker *et al.* 2012), thus it was chosen as the perfect candidate to introduce a detectable deuterium signal to the LDs. We show that the D-OA is readily taken up into LDs and can be clearly observed, also resulting in reduction of the cell's endogenous lipid signal (Fig.3C versus 3F, Table 1). Notably, since D-OA is fully deuterated, the observation of a significant CARS intensity at the CH_2 peak in many droplets exhibiting CARS signal at the CD_2 resonance suggests that D-OA is incorporated into LDs as TAGs containing a combination of fatty acids rather than pure D-OA (Fig.3C, Fig.4I and Fig.S1). It is also evident that fatty acids are readily liberated from LDs for oxidation within the mitochondria, demonstrated by the loss of this label over time (Fig.4B and Fig 5, blue triangle). We clearly observe that carbohydrate starvation

almost removes the CD_2 signal whilst greatly reducing the CH_2 signal (Fig.4E and F, and Fig.5, pink triangle), indicating global fatty acid metabolism in the compensatory response. It is notable that the loss of label occurred in eggs in either carbohydrate-deprived or control medium. Hence, even if eggs can take up pyruvate, as well as short chained fatty acids, from the medium they are still active in oxidising fatty acid from LD stores in resting conditions.

When we blocked β-oxidation in eggs using etomoxir, it was surprising that we observed a distinct decrease in the autofluorescent FAD signal (Fig.6A). Such decrease in FAD reflects a shift to the generation of a more reduced redox state as $FADH_2$ is formed (Duchen, 2000). This type of shift has been seen before in mouse egg mitochondria, in response to sperm induced Ca^{2+} increases which increase pyruvate oxidation (Dumollard *et al.* 2004). We also found that a similar autofluorescence decrease occurred when eggs were exposed to high pyruvate plus dichloroacetate, which promotes pyruvate oxidation (Fig S3). This is consistent with the finding that most of the FAD autofluorescence in mitochondria originates from lipoamide dehydrogenase which is part of the pyruvate dehydrogenase complex (Kunz and Kunz, 1985). Hence our data suggests that blocking fatty acid oxidation leads to an almost immediate increase in oxidation of pyruvate, to compensate for the loss of fatty acid oxidation.

A compensatory increase in pyruvate oxidation could explain why we found that etomoxir caused only a brief and transient decrease in ATP levels before recovering to a similar ATP resting level. Luminescence ATP measurements provided more insight as to the identity of this alternative substrate, since inhibition of mitochondrial pyruvate uptake using a cinnamate derivate prevented the recovery of ATP level after etomoxir addition (Fig.7B and 7C(iv)). This clearly suggests that a compensatory increase in pyruvate uptake is responsible for the recovery of ATP level and the decrease in FAD autofluorescence signal seen with removal of fatty acid oxidation. Whole cell ATP measurements lack the dynamic resolution but they still support the live cell luciferase measurements since a significant decrease in ATP content was only seen when a combination of both etomoxir and cinnamate was used to block both fatty acid and pyruvate oxidation. It was notable that change in FAD fluorescence or in live cell ATP measurements (in the presence of cinnamate) were both substantial and represented about 40% of the total signal that could be attributed to mitochondrial function. Hence these data suggest that mitochondrial oxidation of pyruvate and fatty acids are in a reciprocal balance in mouse eggs, with fatty acids contributing half of the energy required for ATP generation under resting conditions. This balance resembles the Randle cycle described for the reciprocal balance between fatty acid and glucose oxidation in somatic cells (Randle *et al.* 1963). The egg and early embryo variant of the Randle cycle would be between fatty acids and pyruvate with the control point presumably exerted by the levels of acetyl coA inside the mitochondria.

There is previous evidence for a reciprocal balance between pyruvate and fatty acid oxidation in mouse eggs or early embryos. For example etomoxir inhibition of β-oxidation causes an increase in pyruvate dehydrogenase (PDH) complex activity (Bryson *et al.* 1996). O_2 consumption is also seen to continue in the absence of pyruvate (Butcher *et al.* 1998). Interestingly, it has also been shown in skeletal muscle and hepatocytes that inhibition of TC protein Complex I (accepting electrons directly from PDH complex-derived NADH) causes an increase in β-oxidation and mobilisation of TAGs from LD storage (Collier *et al.* 2006; Owen *et al.* 2000).

Neither pyruvate nor fatty acids appear to be optimal for early embryo development. Previous etomoxir studies prove that β-oxidation is required (Dunning *et al.* 2010; Downs *et al.* 2009; Merrill *et al.* 2002), while egg pyruvate-starvation has been shown to result in reduced fertilisation and a reduction in ATP (Dumollard *et al.* 2004; Collado-Fernandez *et al.* 2012). It is also clear that excessive pyruvate or fatty acid oxidation leads to excessive production of ROS (Dumollard *et al.* 2009). It is possible that a 'balanced diet' of pyruvate and β-oxidation helps maintain a low level of metabolism of each substrate, such that the overall metabolic activity of the egg is kept low. This is in accordance with the 'quiet embryo hypothesis' or 'Goldilocks Principle' which state that the optimal level of metabolism within the developing egg or embryo is 'just right' i.e. not too low that development is compromised and not too high that over-production of ROS results (Leese *et al.* 2016). We propose that a low level of both pyruvate and fatty acid oxidation are maintained in order to reduce the excess ROS that are generated under conditions of high metabolic activity.

Together our data demonstrate that mitochondrial pyruvate and fatty acid oxidation in mouse eggs are in balance, and are able to compensate for the loss of the other. It is clear that β-oxidation contributes substantially to the mitochondrial production of ATP, however it appears that it is not critical in maintaining ATP. This suggests that β-oxidation has an alternative important role in development. We also show that we can image fatty acid turnover in live cells, using a unique microscopy method compatible with egg and embryo viability (Bradley *et al.* 2016). Thus, it may be possible to correlate LD distribution with the pattern of metabolism or developmental potential of eggs and early embryos.

Experimental Methods

Gamete Collection and Culture

4-6 week old female MF1 or 8 week old CD1 mice were intraperitoneally injected with 5IU pregnant mare's serum gonadotrophin (PMSG) to induce ovarian follicle development. They were again injected with 10IU human chorionic gonadotrophin (hCG) approximately 48hrs later to induce ovulation. Ovulated mature (MII) eggs were collected from oviducts approximately 15hrs later. Immature germinal vesicle (GV) stage eggs for *in vitro* maturation (IVM) were collected from the

punctured ovarian follicles of un-injected mice. Cumulus cells were removed by gentle pipetting (GV) or brief exposure to hyaluronidase (MII). All animals were handled according to UK Home Office regulations, and procedures carried out under a UK Home Office Project License with approval by Cardiff University Animal Ethics Committee. Eggs from MF1 mice were used throughout the main paper, with Supplementary data in S2 and S3 using eggs from CD1 mice.

All eggs were kept in drops of M2 medium (embryo-tested, Sigma) at 37ºC. β-oxidation was inhibited in MII eggs by the addition of Etomoxir (Sigma) to M2 and culturing for ~6 hours prior to imaging. Carbohydrate starvation was carried out by incubating MII eggs in HEPES-buffered KSOM media containing 3mg/ml bovine serum albumin (BSA, both Sigma) lacking pyruvate, lactate, glutamine, and glucose, also for ~6 hours prior to imaging. Deuterated oleic acid (D-OA) (oleic acid-d_{34}, Sigma) bound to fatty acid-free BSA (Sigma) was introduced to eggs during *in vitro* maturation (IVM) of GV eggs in Minimum Essential Media (MEM, Sigma) containing 400μM D-OA and 3mg/ml BSA for ~18 hours overnight. All drops covered with mineral oil (embryo-tested, Sigma), to prevent evaporation.

CARS and DIC Microscopy

Live eggs were pipetted into a drop of M2 medium in an in-house-built imaging dish with a bottom 25mm round glass coverslip and a removable glass lid. The drop of M2 was maintained at 37ºC and covered in oil to prevent evaporation. The CARS microscope was set up as described by Pope *et al.* (2013), with DIC imaging capabilities. Briefly, CARS excitation fields are obtained by spectrally separating broadband 5fs laser pulses with an appropriate sequence of dichroic beam splitters, resulting in a pump (Stokes) beam with centre wavelength at 682 nm (806 nm) and a bandwidth of 65 nm (200 nm). Spectral focusing through linear chirping of the pump and Stokes fields results in pulse durations of ~1 ps and ~4 ps respectively, achieving a high spectral resolution of 10 cm^{-1}. The excitation pulses are recombined and directed via a home-built beam-scanning head into a Nikon Ti-U inverted microscope. A 1.27 NA x60 water immersion objective (Nikon λS series) and a 0.72 NA dry condenser equipped with DIC optics were used, providing high spatial resolution (0.3 μm lateral, 0.6 μm axial as CARS intensity point-spread function) and forward-CARS collection efficiency.

A monochrome ORCA-285 Hamamatsu CCD camera was used for DIC imaging. A motorised sample stage enabled lateral *xy* sample movement, and axial *z* movement for focussing was enabled by a motorised z-drive (Prior ProScan III). CARS at the anti-Stokes frequency is selected by an appropriate band-pass filter (Semrock) and detected by a photomultiplier tube (Hamamatsu H7422-40). Filters transmitting the 542-582nm wavelength range were used for imaging the CH_2 stretch resonance, allowing detection of wavenumbers in the range of 3,787cm- 2,519 cm^{-1}. A filter transmitting 573-613nm was used for imaging the CD_2 stretch resonance within 2950-1650cm^{-1}. Single-frequency CARS images were obtained at 2850cm^{-1} for the CH_2 stretch vibration. When acquiring CARS images

in the CD_2 mode, sequential images were taken at 2140cm^{-1} and 2850cm^{-1} (i.e. closest to the CH_2 peak when using the 573-613nm CD_2 filter) at each z position, in order to provide both CD_2 and CH_2 data from each egg.

3D z-stacks of CARS images were taken over a 50µm depth of the egg in 0.5µm steps, from -25µm to 25µm (0µm being approximately equatorial). CARS images in *xy* were taken with 0.1µm pixel size, typically in an 80µm x 80µm frame, with 0.01ms pixel dwell time, and time-average total power of ~20mW at the sample. MultiCARS software (in-house developed) allowed collection and regularisation of images from the CARS microscope. Image stacks were assembled into maximum intensity projections and depth colour-coded projections using ImageJ.

To correct for the varying temporal overlap of pump and Stokes at different wavenumbers between CD_2 and CH_2 measurements, the non-resonant CARS intensity of glass under the excitation and detection conditions for each image was used. The CARS intensities measured at the CH_2 peak were then multiplied by the ratio of the non-resonant CARS intensity of glass between the CD_2 and CH_2 peak, in order to provide the value that would have been measured under identical excitation and detection conditions, for direct comparison.

3D z-stacks of DIC images were taken over the full depth of the egg (~70µm) in 0.5µm steps, with 20 ms frame exposure time, using the MicroManager software. A 12.5º polarisation angle in the de-Senarmont DIC illuminator yields a 25º phase offset, found to be sufficiently small to enable good image contrast and sufficiently high to enable quantitative analysis of small phase objects such as lipid membranes (McPhee *et al.* 2013).

LD Aggregate Analysis

The in-house developed CCDPlot software allowed the 3D coordinates, x,y,z widths, and amplitude peaks of LDs from single-frequency CARS images to be found, as described in Bradley *et al.* (2016). Using these coordinates 'clusters' were defined when the LD centre spatial position was within a distance of 1.5 x the resolution (0.3µm laterally, 0.6µm axially) to that of the nearest neighbouring droplet (Fig.2J) (also described by Bradley *et al.*). In order to compare mean aggregate sizes across different developmental stages, the probability P_k of each size k=1, 2, 3… (including size 1. i.e. isolated LDs) was calculated from the histogram (Fig.2G-H) of the aggregate size, as $P_k=O_k/N$, where N is the total number of LDs and O_k is the occurrence of size k. The mean square size was then calculated as $\langle s^2 \rangle = \sum_{k=1}^{+\infty} (k-1)^2 P_k$ for each egg (where we subtracted 1 to obtain the number of partner LDs in an aggregate). Origin was used to plot the square root of the mean square aggregate size (i.e.$\sqrt{\langle s^2 \rangle}$) for all eggs under an experimental condition, against their total number of LDs.

LD D-OA Lipid Volume Analysis

To calculate the average D-OA lipid volume in μm^3 per LD we first find the LD volume by multiplying the LD widths in x,y,z as obtained from CCDPlot analysis. The amplitude of the CARS signal at $2140cm^{-1}$ obtained for each LD (A_i, square root of the CARS intensity) was normalised to a constant amplitude of the brightest droplet in a control D-OA egg (A_b) using A_i/A_b, in order to define relative D-OA densities and compare lipid volumes across conditions. The normalised LD amplitude was then multiplied by the LD volume to calculate the normalised D-OA lipid volume per LD.

In order to compare the average LD D-OA volume across different conditions, the probability (P_{Vi}) of each D-OA volume (v_i) was calculated from the histogram of the normalised D-OA volumes. We used $P_{vi} = O_{vi}/O$, where $O = \sum O_{vi}$ and O_{vi} is the occurrence of volume v_i . The mean volume was then calculated as $\langle v \rangle = \sum(v_i\, P_{vi})$ for each egg. Origin was used to plot the $\langle v \rangle$ for all eggs under an experimental condition, against their total number of LDs.

FAD autofluorescence Assay of Redox Potential

Epifluorescence measurements of FAD autofluorescence were performed using a Nikon Ti-U microscope. Excitation light was provided by a halogen lamp and a Photometrics CoolSnap HQ2 CCD camera was used to collect fluorescence data. A 460nm excitation filter (10nm bandpass) and 510-550nm emission filter were used, alongside a 505nm dichroic mirror. Eggs were briefly exposed to acid Tyrode's solution (Sigma) to remove the zona pellucida allowing them to stick to the microscope dish, to minimise disturbance during addition of experimental chemical treatments to the surrounding media. A perfusion apparatus was set up in order to replace imaging media with fresh media throughout experiments requiring addition of multiple drugs with opposing mechanisms. InVivo software was used to collect data, ImageJ was used to collect data per egg using the MultiMeasure Plug-in, selecting regions of interest. SigmaPlot and Origin were used for normalisation and plotting of data. Graphs were normalised by: $\frac{x_0 - x_{min}}{x_{max} - x_{min}}$ where x_0 is the resting fluorescence level before drug addition, and x_{min} and x_{max} are the minimum and maximum fluorescence levels reached, respectively. This allowed calculation of the contribution of β-oxidation to the redox potential. The intensity of fluorescence emission is presented in arbitrary units.

Luminescence Assays of ATP

A live-cell luciferase assay of ATP was performed by microinjecting MII eggs with either click-beetle luciferase RNA (~1μg/ml) or firefly luciferase protein (10μg/ml). Injections were performed within a shallow drop of M2 under mineral oil to prevent evaporation, upon an unheated microscope stage (Nikon TE2000). Injection needles are pulled on vertical puller (P-30, Sutter Instruments) and connected to an intracellular amplifier (Cyto721, WPI). A Picopump (WPI Ltd), operated by a foot

pump, is used to provide a short pressure pulse of ~20psi, in order to introduce a small amount of luciferase to the egg(~3-5% its volume). Eggs were then pipetted into HKSOM medium containing 100µM luciferin, under mineral oil, on the heated stage of a Zeiss Axiovert S100 microscope within a purpose-built dark box. Photek software was used to collect data per ROI; Origin was used for normalisation and plotting of data. Graphs were normalised by: $\frac{x_0 - x_{min}}{x_{max} - x_{min}}$ as described above. The luminescence values in experiments represent the absolute number of measured photon counts per 10 seconds.

A whole-cell assay of ATP level was performed by pipetting individual whole eggs into 200µl CellTiter-Glo® Luminescent Cell Viability Assay reagent (Promega) before measuring the resultant luminescence signal in a home-built luminometer for 5 minutes. Luminescence signal was collected by a cooled S20 photomultiplier tube (Electron Tubes Ltd., UK). The data was collected and plotted data by the Electron Tubes RS232 Photon Counting software, enabling subsequent SigmaPlot analysis. A calibration curve was produced using increasing known concentrations of ATP (1fmol-10pmol) within the same volume of reagent and was used to determine the total amount of ATP per egg (mM values in a 200pl egg). SigmaPlot software was used to plot the mean total ATP per ensemble of eggs +SEMs.

Chemical Treatments

Chemical treatments were added to HKSOM media during luminescence and epifluorescence imaging, while eggs were incubated in different drug combinations for ~1 hour prior to taking whole cell ATP measurements. Etomoxir (Sigma) was added at 100µM final concentration to inhibit β-oxidation. Alpha cyano-4 hydroxycinnamate (referred to as cinnamate, Sigma) was added with a final concentration of 0.5mM, to prevent pyruvate transport into mitochondria. 2mM sodium cyanide (CN^-, Sigma) was used to induce a fully reduced redox state, while uncoupler, FCCP (Carbonyl cyanide-*4*-(trifluoromethoxy)phenylhydrazone) (Sigma) was added to media with a final concentration of 1µM for a fully oxidised redox state. Perfusion of media in the microscope dish with fresh medium throughout measurements allowed the subsequent addition of CN^- and FCCP within the same experiment.

Acknowledgements: Authors would like to thank Dale Boorman for provision of deuterated and non-deuterated oleic acid spectra, and Ros John for advice and discussions.

Conflict of interest: The authors declare that they have no conflicts of interest with the contents of this article.

Funding: J.B. acknowledges financial support by the President's Research Scholarship programme of Cardiff University and the UK BBSRC Research Council responsive mode research grant (grant n. BB/P007511/1). PB acknowledges the UK EPSRC Research Council for her Leadership fellowship award (grant n. EP/I005072/1) and the Royal Society for her Wolfson Research Merit Award (grant n. WM140077). I.P. is funded by the UK EPSRC (grant n. EP/L001470/1) and UK BBSRC (grant n. BB/P007511/1). W.L. acknowledges support by a Leverhulme Royal Society Research Fellowship (Grant No. LT20085).
The CARS microscope set-up was funded by the UK BBSRC [grant BB/H006575/1 and BB/P007511/1].

References

Apparicio, M., Ferreira, C. R., Tata, A., Santos, V. G., Alves, A. E., Mostachio, G. Q., Pires-Butler, E. A., Motheo, T. F., Padilha, L. C., Pilau, E. J., Gozzo, F. C., Eberlin, M. N., Lo Turco, E. G., Luvoni, G. C. and Vicente, W. R. R. (2012). Chemical Composition of Lipids Present in Cat and Dog Egg by Matrix-Assisted Desorption Ionization Mass Spectrometry (MALDI-MS) *Reprod. Dom. Anim.* **47**(6) 113-117

Bergner, G. Albert, C.R., Schiller, M., Bringmann, G., Schirmeister, T., Dietzek, B., Niebling, S., Schlucker, S. and Popp, J. (2011). Quantitative Detection of C-Deuterated Drugs by CARS Microscopy and Raman Microspectroscopy *Analyst* **136** 3686-3693

Bradley, J. (2016) L*abel-free multiphoton microscopy of lipid droplets in oocytes, eggs, and early embryos.* PhD Thesis, Cardiff University.

Bradley, J., Pope, I., Masia, F., Sanusi, R., Langbein, W., Swann, K. and Borri, P. (2016). Quantitative imaging of lipids in live mouse eggsand early embryos using CARS microscopy *Dev.* **143** 2238-2247

Bryson, J.M., Cooney, G.J., Wensley, V.R., Phuyal, J.L., and Caterson, I.D. (1996). The Effects of the Inhibition of Fatty Acid Oxidation On Pyruvate Dehydrogenase Complex Activity in Tissues of Lean and Obese Mice *Int. J. Obes. Relat. Metab. Disord.* **20** 738-744

Butcher, L., Coates, A., Martin, K.L., Rutherford, A.J., and Leese, H.J. (1998). Metabolism of Pyruvate in the Early Human Embryo *Biol. Reprod.* **58** 1054-1056

Collado-Fernandez, E., Picton, H. and Dumollard, R. (2012). Metabolism Throughout Follicle and Egg Development in Mammals *Int. J. Dev. Biol.* **56** 799-808

Collier, C.A., Bruce, C.R., Smith, A.C., Lopschuk, G., and Dyck, D.J. (2006). Metformin Counters the Insulin-Induced Suppression of Fatty Acid Oxidation and Stimulation of Triglycerol Storage in Rodent Skeletal Muscle *Am. J. Physiol. Endocrinol. Metab.* **291** 182-189

Downs, S.M. (1995). The influence of Glucose, Cumulus Cells and Metabolic Coupling On ATP Levels and Meiotic Control in the Isolated Mouse Egg *Dev. Biol.* **167** 502-512

Downs, S.M., Mosey, J.L., and Klinger, J. (2009). Fatty Acid Oxidation and Meiotic Resumption in Mouse Eggs*Mol. Reprod. Dev.* **76** 844–853

Duchen, M.R. (2000). Mitochondria and Calcium: from Cell Signalling to Cell Death *J. Physiol.* **529.1** 57-68

Dumollard, R., Marangos, P., Fitzharris, G., Swann, K., Duchen, M., and Carroll, J. (2004). Sperm-Triggered [Ca^{2+}] Oscillations and Ca2+ Homeostasis in the Mouse Egg have an Absolute Requirement for Mitochondrial ATP Production *Dev.* **131** 3057-3067

Dumollard, R., Ward, Z., Carroll, J., and Duchen, M. (2007). Regulation of Redox Metabolism in the Mouse Egg and Embryo *Dev.* **134** 455-465

Dumollard, R., Campbell, K., Halet, G., Carroll, J., and Swann, K. (2008). Regulation of Cytosolic and Mitochondrial ATP Levels in Mouse Eggs and Zygotes *Dev. Biol.* **316** 431–440

Dumollard, R., Carroll, J., Duchen, M.R., Campbell, K., and Swann, K. (2009). Mitochondrial Function and Redox State in Mammalian Embryos *Semin. Cell. Dev. Biol.* **20** 346–353

Duncan, M. D., Reintjes, J., and Manuccia, T.J. (1982). Scanning Coherent Anti-Stokes Raman Microscope *Opt. Lett.* **7**(8) 350-352

Dunning, K.R., Cashman, K., Russell, D.L., Thompson, J.G., Norman, R.J., and Robker, R.L. (2010). Beta-Oxidation is Essential for Mouse Egg Developmental Competence and Early Embryo Development *Biol. Reprod.* **83** 909–918

Dunning, K.R., Akison, L.K., Russell, D.L., Norman, R.J., and Robker, R.L. (2011). Increased Beta-Oxidation and Improved Egg Developmental Competence in Response to L-Carnitine During Ovarian *in vitro* Follicle Development in Mice *Biol. Reprod.* **85** 548–555

Fu, D., Yu, Y., Folick, A., Currie, E., Farese Jr, R.V., Tsai, T-H., Xie, X.S. and Wang, M.C. (2014). In Vivo Metabolic Fingerprinting of Neutral Lipids with Hyperspectral Stimulated Raman Scattering Microscopy *J. Am. Chem. Soc.* **136** 8820-8828

Gardner, D.K. and Leese, H.J. (1986). Non-invasive Measurement of Nutrient Uptake by Single Cultured Pre-implantation Mouse Embryos *Hum. Reprod.* **1**(1) 25-27

Homa, S.T., Racowsky, C. and McGaughey, R.W. (1986). Lipid Analysis of Immature Pig Eggs*J. Reprod. Fert.* **77** 425-434

Kunz, W.S. and Kunz W. (1985) Contribution of different enzymes to flavoprotein fluorescence of isolated rat liver mitochondria. Biochem. Biophys. Acta **841**, 237-246

Leese, H. (2002). Quiet Please, Do Not Disturb: A Hypothesis of Embryo Metabolism and Viability *Bioessays* **24** 845-849

Leese, H. J., Guerif, F., Allgar, V., Brison, D., Lundin, K. and Sturmey, R. (2016). Biological Optimization, the Goldilocks Principle, and How Much is Lagom in the Preimplantation Embryo *Mol. Reprod. Dev.* **83** 748-754

McEvoy, T.G., Coull, G.D., Broadbent, P.J., Hutchinson, J.S.M. and Speake, B.K. (2000) Fatty acid composition of lipids in immature cattle, pig and sheep oocytes with intact zona pellucida. *J. Reprod. Fertil.* **118,** 163-170

McPhee, C.I., Zoriniants, G., Langbein, W., and Borri, P. (2013). Measuring the Lamellarity of Giant Lipid Vesicles with Differential Interference Contrast Microscopy *Biophys. J.* **105**(6) 1414-1420

Merrill, C.L., Ni, H., Yoon, L.W., Tirmenstein, M.A., Narayanan, P., Benavides, G.R., Easton, M.J., Creech, D.R., Hu, C.X., McFarland, D.C., Hahn, L.M., Thomas, H.C. and Morgan, K.T. (2002). Etomoxir-Induced Oxidative Stress in HepG2 Cells Detected by Differential Gene Expression is Confirmed Biochemically *Toxicol. Sci.* **68** 93-101

Owen, M.R., Doran, E., and Halestrap, P. (2000). Evidence That Metformin Exerts Its Anti-Diabetic Effects Through Inhibition of Complex I of the Mitochondrial Respiratory Chain *Biochem.. J.* **348** 607-614

Pope, I., Langbein, W., Watson, P. and Borri, P. (2013). Simultaneous Hyperspectral Differential-CARS, TPF, and SHG Microscopy with a Single 5fs Ti:Sa Laser *Opt. Express* **21**(6) 7096-7106

Potma, E.O. and Xie, X.S. (2004). CARS Microscopy for Biology and Medicine *Opt. Photonics News* **15**(11) 40-45

Randle, P.J., Hales, C.N., Garland, P.B. and Newsholme, E.A. (1963). The Glucose Fatty-Acid Cycle: Its Role in Insulin Sensitivity and the Metabolic Disturbances of Diabetes Mellitus *Lancet* **1**(7285) 785-789

Rodriguez, L.G., Lockett, S.J. and Holtom, G.R. (2006). Coherent Anti-Stokes Raman Scattering Microscopy: A Biological Review *Cytom. Part A* **69A** 779-791

Shaaker, M., Rahimipour, A., Nouri, M., Khanaki, K., Darabi, M., Farzadi, L., Shahnazi, V. and Mehdizadeh, A. (2012). Fatty Acid Composition of Human Follicular Fluid Phospholipids and Fertilization Rate in Assisted Reproductive Techniques *Iran. Biomed. J.* **16**(3) 162-168

Sturmey, R.G. and Leese, H.J. (2003). Energy Metabolism in Pig Eggsand Early Embryos *Reprod.* **126** 197-204

Zhang, D., Slipchenko, M.N. and Cheng, J-X. (2011). Highly Sensitive Vibrational Imaging by Femtosecond Pulse Stimulated Raman Loss *J. Phys. Chem. Lett.* **2** 1248-1253

Walther, T.C. and Farese, R.V. (2012). Lipid Droplets and Cellular Metabolism. *Ann. Rev. Biochem*. 81, 687-714.

Figures

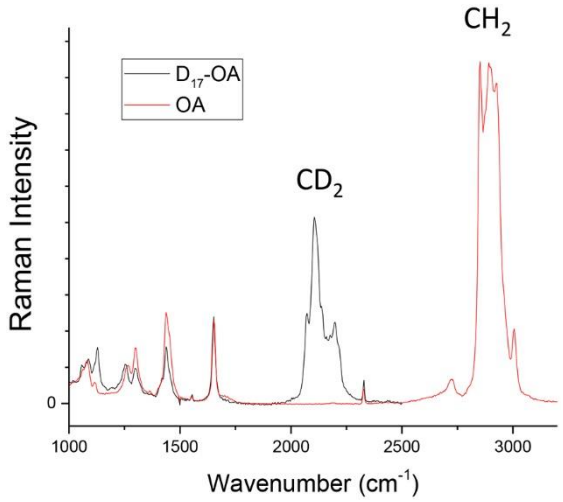

Figure 1. Raman spectra of deuterated and non-deuterated oleic acid

Raman spectrum showing the vibrational resonances of the CD_2 bond in deuterated oleic acid (D_{17}-OA) at ~2100cm^{-1} and the CH_2 bond in (un-deuterated) oleic acid at 2850cm^{-1}. The CD_2 bond lies in the spectrally silent region, where no vibrational modes are present for the un-deuterated compound, allowing for its distinct detection.

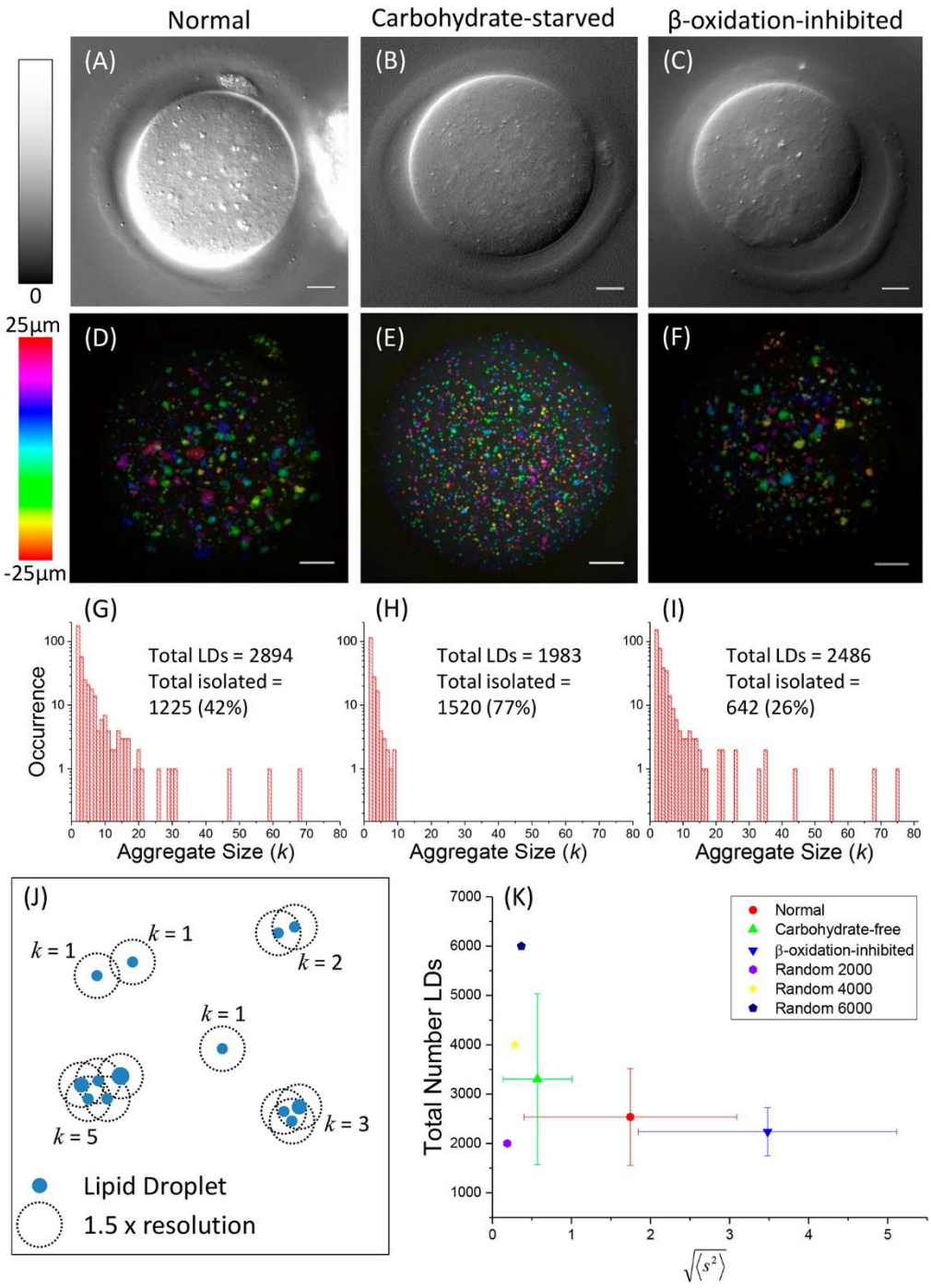

Figure 2. Lipid Droplet Aggregation Patterns in MII Eggs with Altered Mitochondrial Metabolism

Column 1, MII egg incubated in simple M2 medium (n=30), Column 2, carbohydrate-starved MII egg (n=8), Column 3, β-oxidation-inhibited MII egg (100µM etomoxir) (n=6). (A-C) Single-plane (approximately equatorial) DIC images using a 1.27 NA water objective and a 0.72 NA dry condenser. (D-F) depth colour-coded images of CARS z-stacks at wavenumber 2850cm^{-1} (CH_2 vibration) through the same MII eggs. 0.1x0.1µm xy pixel size; 0.5µm z-step; 0.01ms pixel dwell time; ~14mW (~9mW) Pump (Stokes) power at the sample. Scale bars represent 10µm; colour bar

shows depth colour-coding from -25µm to 25µm of 101 z-stacks (0µm = approximately equatorial plane), the brightness of each colour is the maximum intensity at each corresponding z-plane. (G-I) Representative histograms of the number of LDs making up clusters for the different growth conditions above. (J) Cartoon illustrating the determination of LD cluster size. (K) Scatter plot of the square root of the mean squared cluster size ($\sqrt{\langle s^2 \rangle}$) against the total number of LDs. The aggregation pattern of 2000, 4000 and 6000 random 'droplets' is also shown. The distribution of each variable in the corresponding ensemble is shown as an average (symbol) and standard deviation (bar). Data is from multiple trials, using 2-3 mice for each.

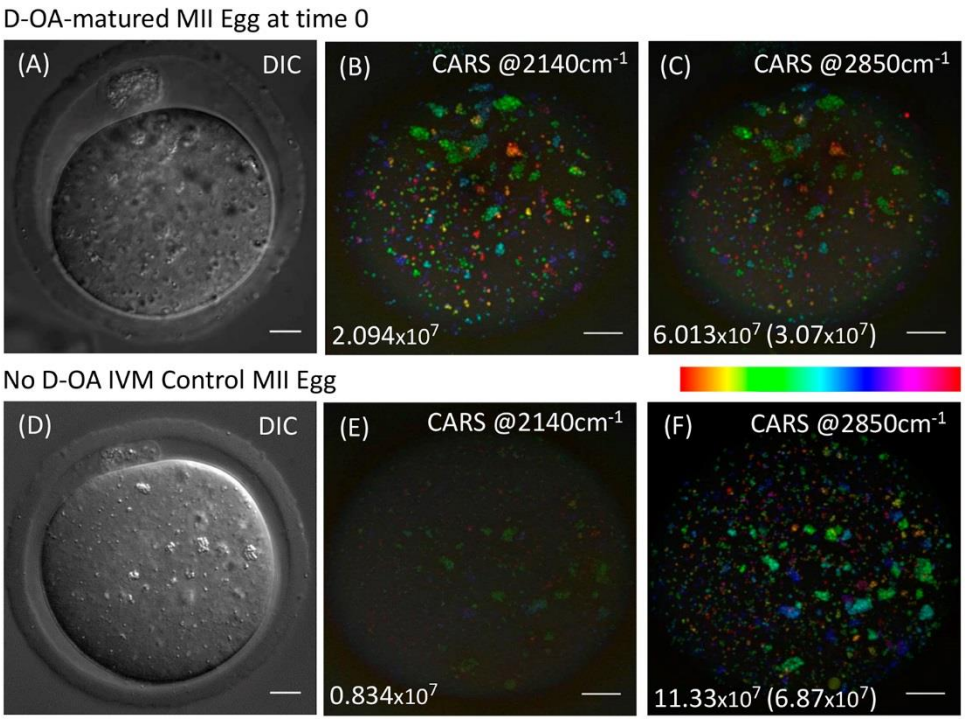

Figure 3. CARS imaging of Eggs incubated with Deuterated Oleic Acid

Single-plane (approximately equatorial) DIC images using a 1.27 NA water objective and a 0.72 NA dry condenser, and depth colour-coded images of CARS z-stacks at wavenumbers 2140cm^{-1} (CD_2 vibration) and 2850cm^{-1} (CH_2 vibration) through the same MII eggs, showing deuterium-labelled oleic acid (D-OA) in LDs. (A-C) MII egg in vitro matured with 400µM D-OA (n=5), (D-F) control MII egg in vitro matured without D-OA (n=3). Maximum CARS intensities are shown in photoelectrons per second, with the values in parenthesis in (C) and (F) denoting the intensity under the same excitation conditions as (B) and (E), i.e. corrected for the varying temporal overlap of pump and Stokes at different wavenumbers. (B) and (E) are scaled to the brightness of (B); (C) and (F) are scaled to the brightness of (F). 0.1x0.1µm xy pixel size; 0.5µm z-step; 0.01ms pixel dwell time; ~14mW (~9mW) Pump (Stokes) power at the sample. Scale bars represent 10µm; colour bar shows depth colour-coding from -25µm-25µm of 101 z-stacks (0µm being the approximately equatorial plane of the egg). Data is from multiple trials, using 2-3 mice for each.

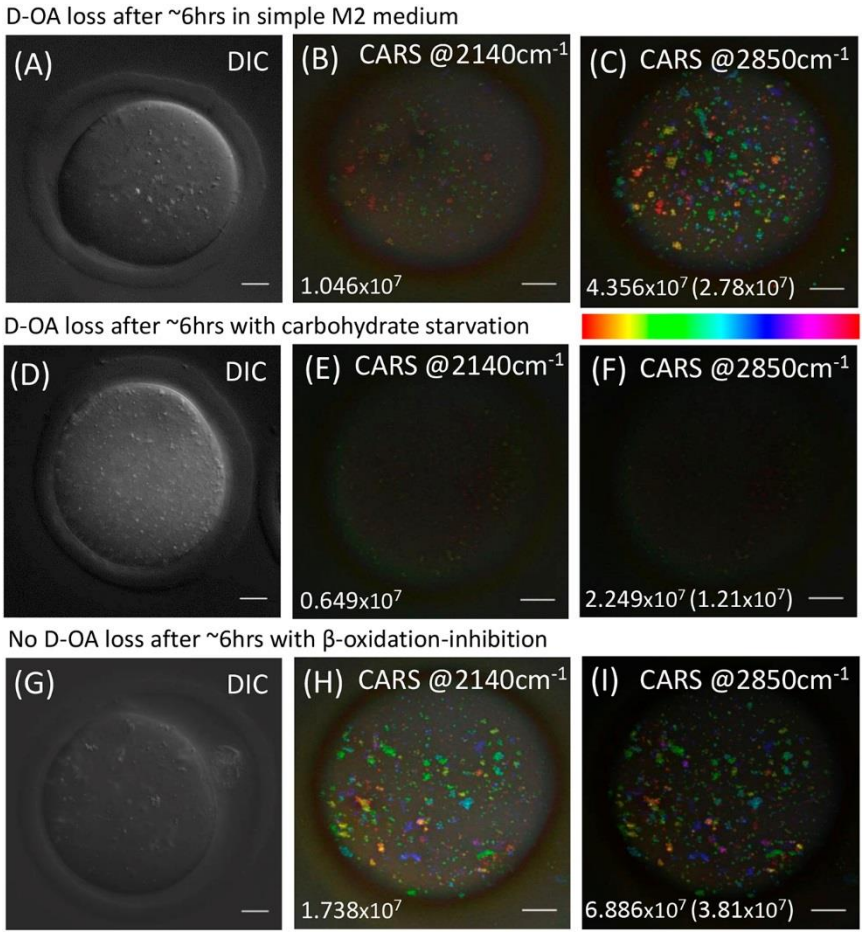

Figure 4. Loss of Deuterated Oleic Acid in Eggs with Altered Mitochondrial Metabolism

Single-plane (approximately equatorial) DIC images using a 1.27 NA water objective and a 0.72 NA dry condenser, and depth colour-coded images of CARS z-stacks at wavenumbers 2140cm^{-1} (CD_2 vibration) and 2850cm^{-1} (CH_2 vibration) through the same MII eggs, showing deuterium-labelled oleic acid (D-OA) in LDs after 6hrs in a representative (A-C) egg incubated in simple M2 medium (n=4), (D-F) carbohydrate-starved egg (n=8), (G-I) β-oxidation-inhibited egg (100μM etomoxir) (n=6). Maximum CARS intensities are shown in photoelectrons per second, with the values in parenthesis in (C) (F) and (I) denoting the intensity under the same excitation conditions as (B) (E) and (H), i.e. corrected for the varying temporal overlap of pump and Stokes at different wavenumbers. (B) (E) and (H) are scaled to the brightness of (H); (C) (F) and (I) are scaled to brightness of (I). 0.1x0.1μm xy pixel size; 0.5μm z-step; 0.01ms pixel dwell time; ~14mW (~9mW) Pump (Stokes) power at the sample. Scale bars represent 10μm; colour bar shows depth colour-coding from -25μm-25μm of 101 z-stacks (0μm being the approximately equatorial plane of the egg). Data is from multiple trials, using 2-3 mice for each.

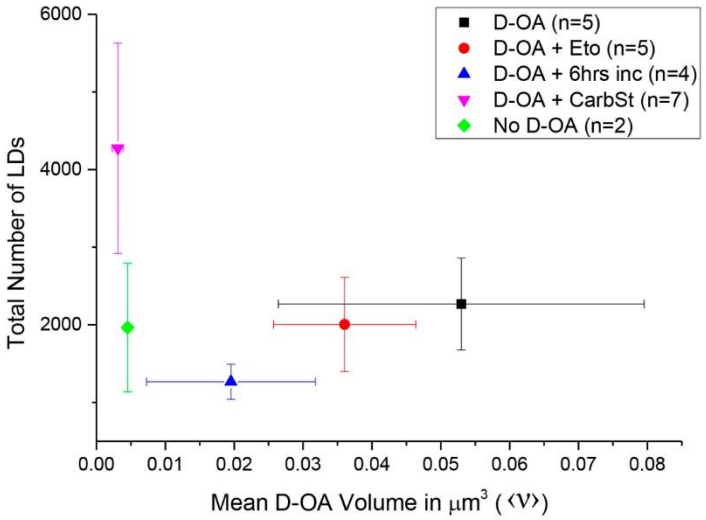

Figure 5. Deuterated Oleic Acid Content of Eggs with Altered Mitochondrial Metabolism

Mean D-OA lipid volume in μm^3 ($\langle v \rangle$) against total number of LDs in ensembles of control MII eggs imaged immediately after overnight incubation with D-OA (black square, n=5), MII eggs incubated in etomoxir for 6hrs after incubation with D-OA (red circle, n= 5), MII eggs incubated in M2 media for 6hrs after incubation (blue triangle, n=4), MII eggs incubated in pyruvate, lactate and glutamate-free media for 6hrs after incubation with D-OA (pink inverted triangle, n=7), and MII eggs not incubated with D-OA (green diamond, n=2). The distribution of each variable in the corresponding ensemble is shown as an average (symbol) and standard error of the mean (bar). Data is from multiple trials, using 2-3 mice for each.

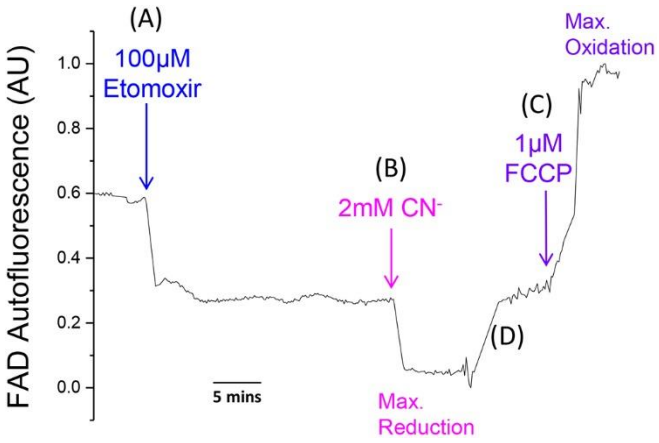

Figure 6. FAD Autofluorescence Imaging of Mitochondrial Redox Potential

Mitochondrial FAD autofluorescence signal in MII eggs subjected to (A) β-oxidation inhibition (100μM etomoxir), followed by (B) induction of maximum reduction (2mM cyanide) and (C) subsequent maximum oxidation (1μM FCCP), following a (D) perfusion washing step (n=15). Data is representative of multiple trials, using 2-3 mice for each.

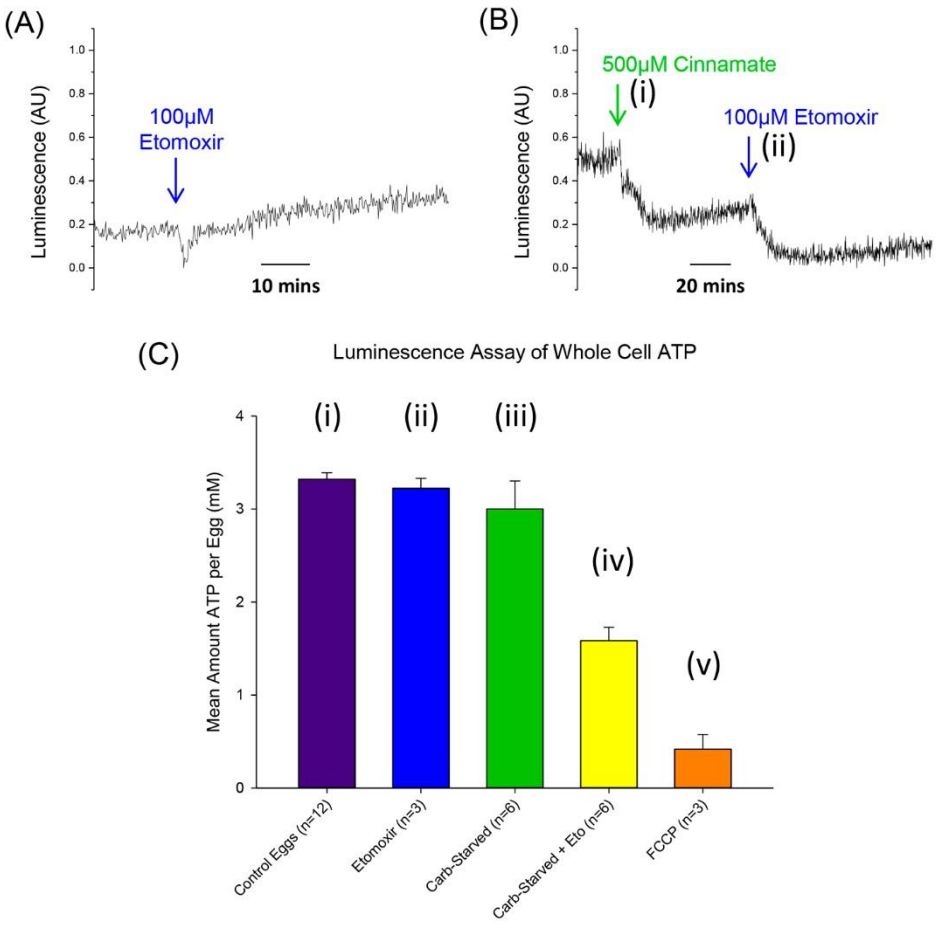

Figure 7. Luminescence imaging of ATP with Altered Mitochondrial Metabolism

(A and B) Live-cell luciferase imaging of change in ATP production in response to (A) β-oxidation inhibition (100µM etomoxir) (n=12), (B) pyruvate-uptake inhibition (500µM cinnamate) and subsequent β-oxidation inhibition (100µM etomoxir) (n=13). (C) Histogram of average whole cell ATP measurements in ensembles of MII eggs, (i) incubated in simple M2 medium (n=12), (ii) β-oxidation-inhibited eggs (100µM etomoxir) (n=3), (iii) carbohydrate-starved eggs (modified incubation medium or treated with 500µM cinnamate) (n=6), (iv) eggs subjected to carbohydrate-starvation and β-oxidation-inhibition (modified incubation medium and 100µM etomoxir or treated with 500µM cinnamate and 100µM etomoxir) (n=6), (v) and eggs treated with 1µM FCCP (n=3). Luminescence measurements were taken after 1 hour of treatment. SEMs shown. Data is representative of or from multiple trials, using 2-3 mice for each.

Table 1. CARS Maximum intensity and Mean D-OA Volume per LD ($\langle v \rangle$) in Eggs with Altered Mitochondrial Metabolism

	CD_2 Signal @2140cm^{-1} (x10^7 ph.e^-/sec)	CH_2 Signal @2850cm^{-1} (x10^7 ph.e^-/sec, corrected – see methods)	Mean D-OA volume per LD ($\langle v \rangle$) ±SEM (μm^3 x10^{-2})
Control No D-OA Incubated Egg at time 0	0.83	6.87	0.45 ± 0.04
Control 400µM D-OA Incubated Egg at time 0	2.09	3.07	5.3 ± 2.7
400µM D-OA Incubated Egg Imaged after 6hrs in normal media	1.05	2.78	2.0 ± 1.2
400µM D-OA Incubated Egg Imaged after 6hrs in carbohydrate-starvation media	0.65	1.21	0.31 ± 0.08
400µM D-OA Incubated Egg Imaged after 6hrs in β-oxidation inhibition media	1.74	3.81	3.6 ± 1.0

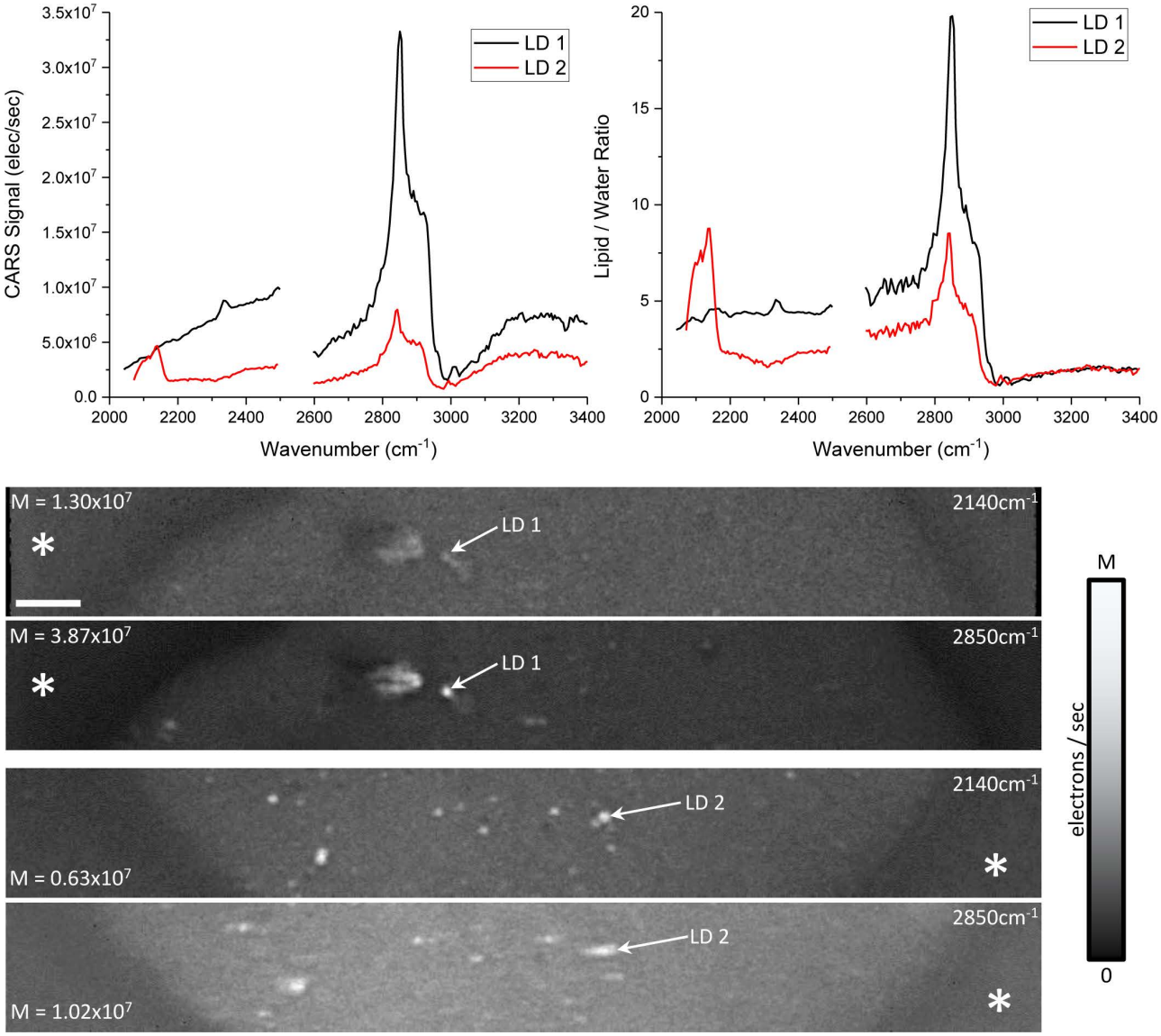

Figure S1. Lipid droplet spectrum (averaged over a single droplet, as indicated in images) taken from two different MII eggs incubated in etomoxir for 6hrs after incubation with D-OA. Graph top left, CARS signal averaged across lipid droplet. Graph top right, lipid/water ratio. Water signal was averaged in the region identified by the * in images. CARS images at the frequencies 2140 cm-1 and 2850 cm-1 showing the location of the lipid droplets used to plot the spectra in the above graphs. M indicates the grey scale range, in electrons per second, over which the images are plotted. Scale bar equals 5 microns.

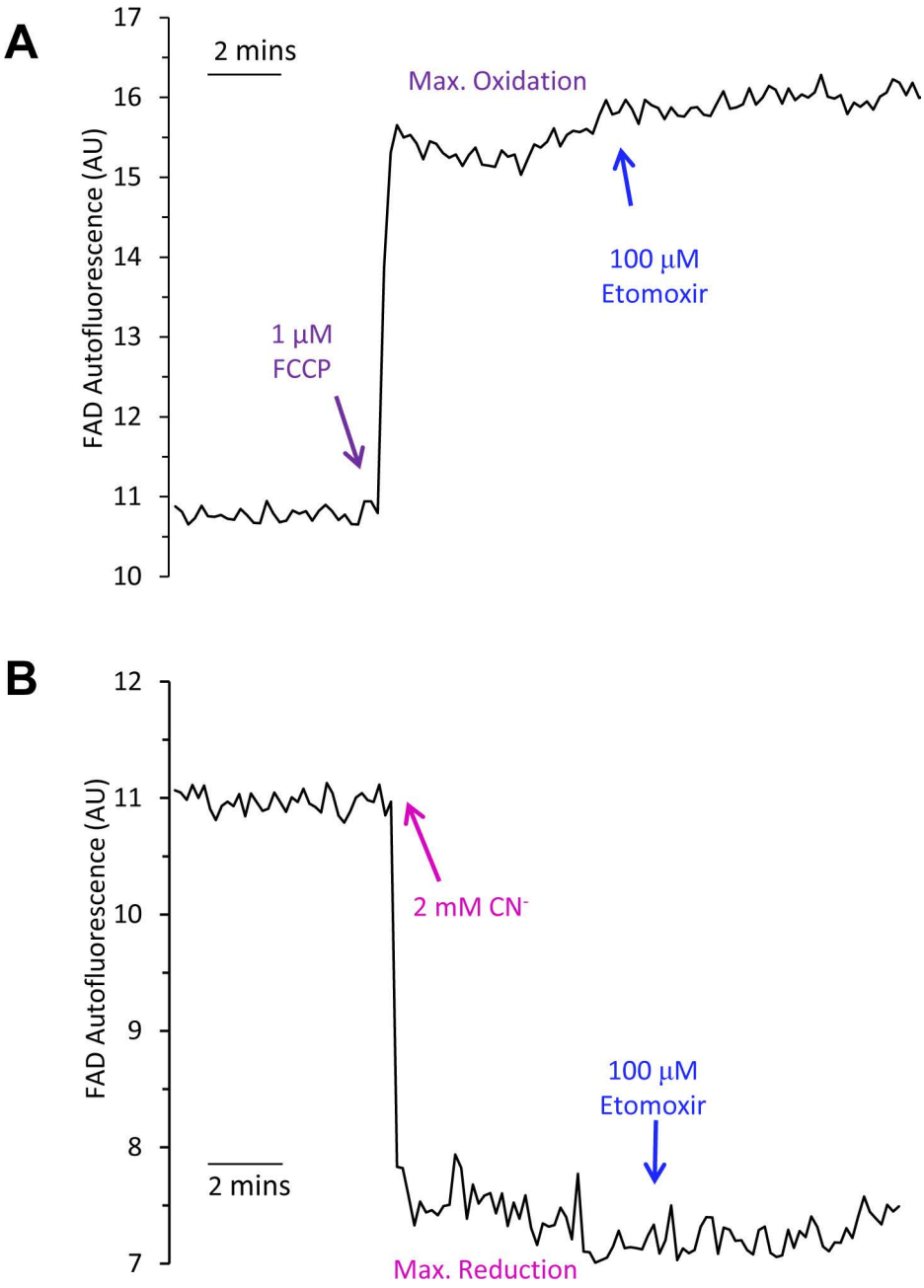

Figure S2. Etomoxir on FAD autofluorescence in mouse eggs.
Mitochondrial FAD autofluorescence signals in MII eggs incubated and imaged in standard HKSOM media. In **A** the eggs were subjected to exposed 1 µM FCCP to cause maximum oxidation, followed by addition of 100 µM etomoxir (n = 9). In **B** the addition of 2mM cyanide was added to cause maximum reduction, followed by addition of 100 µM etomoxir (n=9). All data is representative of multiple trials, using 2-3 mice for each. In neither type of experiment did etomoxir cause a change in autofluorescence.

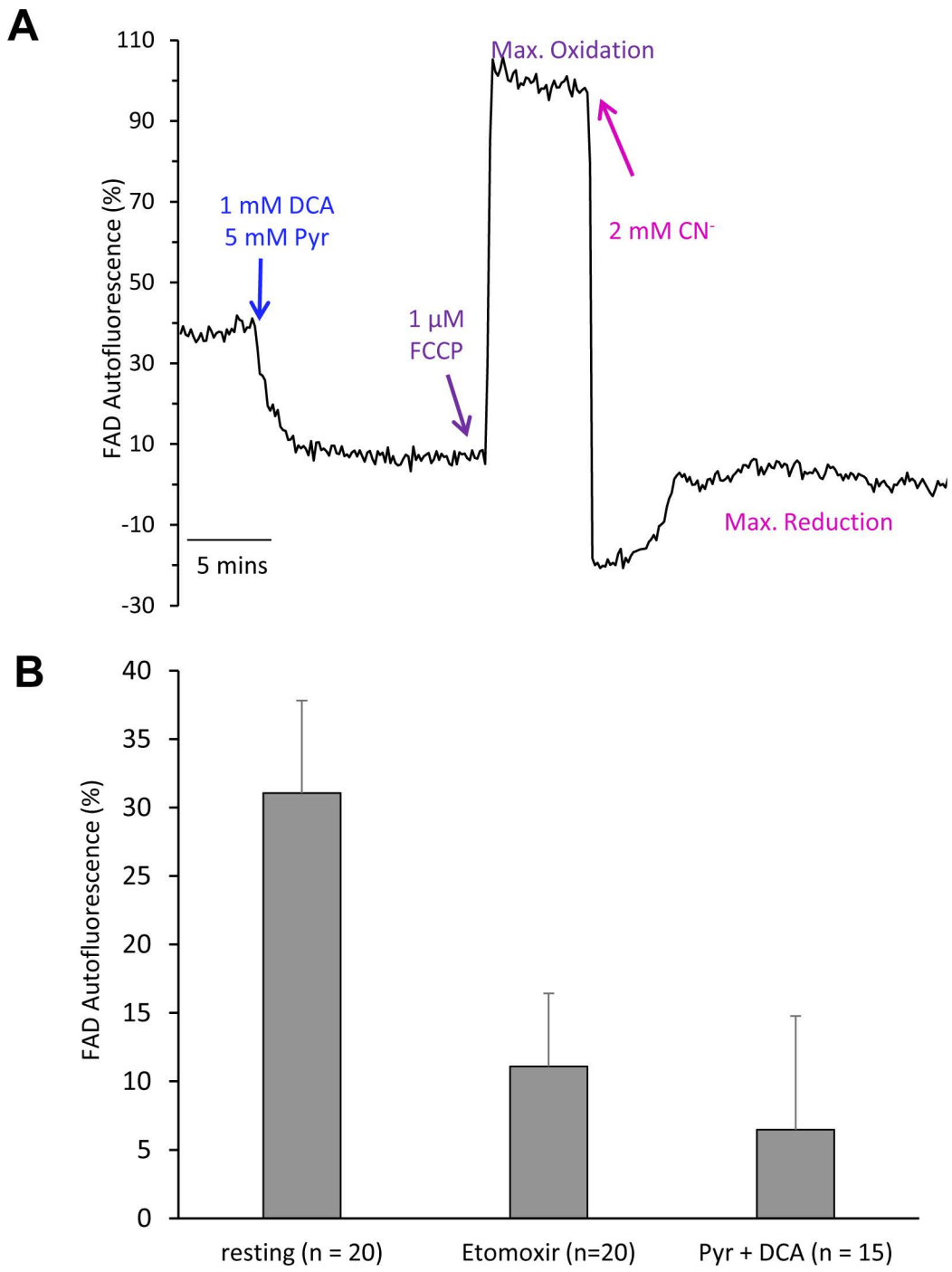

Figure S3. Effects of Pyruvate Intake On Mitochondrial Redox Potential of FAD in MII eggs. In **A** the mitochondrial FAD autofluorescence signal was measured from MII eggs in standard HKSOM media. Then eggs were exposed to 1 mM dichloroacetate (DCA) plus 5 mM pyruvate which caused a decrease in FAD autofluorescence. This was followed by maximum oxidation (1 µM FCCP) and induction of maximum reduction (2 mM cyanide) (n=15). Data is representative of multiple trials, using 2-3 mice for each. In **B** the average mitochondrial redox potentials are shown based upon FAD auto-fluorescence measurements. All eggs were incubated and imaged in standard HKSOM media. The resting state is that seen at the start of the experiment, then the average is shown for eggs treated with 100 µM etomoxir, and finally the level is shown for that seen after adding 1 mM DCA and 5 mM pyruvate.